Published in final edited form as:
Invest Ophthalmol Vis Sci. 2009 September ; 50(9): 4386–4393. doi:10.1167/iovs.09-3471.

Retinal Pigment Epithelium Defects in Humans and Mice with Mutations in *MYO7A*: Imaging Melanosome-Specific Autofluorescence

Daniel Gibbs[*,1,2], **Artur V. Cideciyan**[3], **Samuel G. Jacobson**[3], and **David S. Williams**[*,1,2]

[1]Department of Pharmacology, UCSD School of Medicine, La Jolla, California

[2]Department of Neurosciences, UCSD School of Medicine, La Jolla, California

[3]Department of Ophthalmology, Scheie Eye Institute, University of Pennsylvania, Philadelphia, Pennsylvania

Abstract

PURPOSE—Usher syndrome (USH) is a genetically heterogeneous disease with autosomal recessive deafness and blindness. Gene therapy is under development for use in the most common genetic variant of USH1, USH1B, which is caused by mutations in the *MYO7A* gene. This study was undertaken to identify an imaging method for noninvasively monitoring the RPE component of the USH1B disease.

METHODS—NIR-autofluorescence (NIR-AF) was examined in USH1B patients with scanning laser ophthalmoscopy, and retinal thickness with spectral-domain optical coherence tomography. *Myo7a*-null mouse retinas and purified RPE melanosomes were analyzed by spectral deconvolution confocal microscopy.

RESULTS—In USH1B patients, NIR-AF was normal in regions of retained photoreceptors and abnormal in regions lacking photoreceptors. Subtle changes in NIR-AF were associated with intermediate photoreceptor loss. In ex vivo mouse retinas, the NIR-AF source was traced to the melanosomes in the RPE and choroid. Purified RPE melanosomes emitted the same signal. Fluorophores, excited by long-wavelength light, were evident throughout the apical RPE of WT mouse eyecups. In *Myo7a*-null eyecups, these fluorophores had a more restricted distribution. They were absent from the apical processes of the RPE, thus correlating with the melanosome localization defects described previously by conventional microscopy.

CONCLUSIONS—The data indicate that melanosomes in the RPE and choroid are the dominant source of NIR-AF from the posterior region of the eye. NIR-AF is a novel tool that provides sensitive and label-free imaging of the retina and RPE and is currently the only melanosome-specific, noninvasive technique for monitoring RPE disease in new therapeutic initiatives for retinal degenerations.

Vision loss in human hereditary retinal degenerations (RDs) is caused mainly by mutations in genes expressed in the photoreceptors, the retinal pigment epithelium (RPE), or both. In the Usher syndromes (USH), mutant genes also lead to inner ear dysfunction and cause debilitating

[*]Each of the following is a corresponding author: Daniel Gibbs, The Salk Institute for Biological Studies, 10010 N. Torrey Pines Road, La Jolla, CA 92037-1099; dgibbs@salk.edu., David S. Williams, Jules Stein Eye Institute, UCLA School of Medicine, 200 Stein Plaza, Los Angeles, CA 90095-7008; dswilliams@ucla.edu.

Disclosure: **D. Gibbs**, None; **A.V. Cideciyan**, None; **S.G. Jacobson**, None; **D.S. Williams**, None

bisensory disease. The success of human gene therapy in retinas of patients with LCA[1–]4 has paved the way for the application of this technique to other blinding disorders, such as the most common form of USH type 1, USH1B, which is caused by mutations in the myosin VIIa (*MYO7A*) gene.[5,6] MYO7A is an unconventional myosin motor protein expressed both in retinal photoreceptors and the RPE.[7,8] In photoreceptors, MYO7A appears to participate in opsin transport through the cilium, whereas in the RPE, one of its functions is in the movement of melanosomes. [9,10] Whether gene therapy of USH1B[11,12] targets photoreceptors or RPE, or both, there is a need to monitor RPE-melanosome disease independent of photoreceptor disease and vision.

RPE forms a thin monolayer between the photoreceptors and their blood supply, the choroid. [13] Noninvasive evaluation of RPE health have depended on the lipofuscin granules found within these cells.14,15 Lipofuscin is a lipid and protein aggregate containing several distinct fluorophores that produce yellow-orange emission spectra when excited by blue light.14–16 Noninvasive imaging methods that take advantage of the autofluorescence (AF) of lipofuscin have enabled mapping and quantification of RPE disease and its progression in living human eyes with retinal degenerative diseases.[15,17–20] However, conventional lipofuscin imaging involves bright short-wavelength illumination that may accelerate the natural history of RDs21 and possibly complicate outcomes of a clinical trial. Reduced short-wavelength illuminance methods are being developed. [20]

RPE cells also contain abundant intracellular pigment granules, which correspond to the last stage of melanosome maturation—a process that starts early during gestation and is practically complete before 2 years of age in humans.[22,23] Melanosomes in the RPE are thought to play a protective role by absorbing radiation, scavenging free radicals and quenching excited molecular states.[22,24] Alternatively or additionally, melanosomes could mediate light-induced toxicity in the RPE.[25] They may also contribute to protein degradation after the phagocytosis of outer segment disc membranes.22,26 Until recently, only indirect methods were available for imaging the abnormalities of melanin, based on absorption and scattering properties.27–30 Recently, a novel AF signal has been observed by noninvasive imaging of living human eyes with near-infrared (NIR) excitation light.[20,31–38] It has been speculated that melanosomes contribute to the NIR-AF signal, but the validity of this hypothesis or the extent of the contribution from different fluorophores has not been defined. In the present study, AF imaging was used in USH1B patients and in *Myo7a*-null shaker1 mice. The results identify melanosomes of the RPE and choroid as the endogenous fluorophores that give rise to the NIR-AF signal and set the stage for further development of NIR-AF imaging to define and monitor subtle melanosome abnormalities in the RPE before and after therapeutic interventions.

MATERIALS AND METHODS

Human Subjects

Patients with USH1B (i.e., with *MYO7A* mutations) were included.[6,30] Subjects P1, P2, and P3 in the current paper correspond to F5,P2, F3,P1, and F14,P1, respectively, in Jacobson et al.[6] Informed consent was obtained; procedures adhered to the Declaration of Helsinki and received institutional review board approval.

Autofluorescence (AF) Imaging with the Confocal Scanning Laser Ophthalmoscope (CSLO)

En face AF imaging was performed in living human eyes with CSLO (HRA2; Heidelberg Engineering GmbH, Heidelberg, Germany) with NIR excitation light at 790 nm and a long-pass blocking filter that allowed detection of fluorescence emissions of >810 nm.[20,33–35] The power of the NIR light measured at the cornea was 2.5 mW. The high-resolution mode of the angiograph was used where 30° × 30° of retina is sampled onto a 1536 × 1536-pixel, image

and 25-frame video sequences were obtained at the rate of 4.7 Hz. Detector sensitivity was set to 95%. The images were exported from the manufacturer's software and analyzed as described.[20,33–35] NIR-AF signal intensity was measured along a 30-pixel-wide (176-μm) profile passing through the foveola and the center of the optic nerve head. Microscope slides with purified melanosomes were imaged with the use of an additional 20-D lens at a working distance of ~10 mm using a focus setting of 52 D. A 15° setting was used at 768 × 768-pixel resolution spanning a field of view of ~5 mm. Off-axis imaging was used to avoid specular reflections from the cover slide. One hundred consecutive frames were obtained and averaged to increase signal to noise ratio.

Cross-sectional Imaging with Optical Coherence Tomography (OCT)

Retinal cross sections were obtained with spectral-domain (SD) OCT imaging (RTVue-100; Optovue Inc., Fremont, CA). The principles of the method and our recording and analysis techniques have been published.[6,34,35,39,40] Briefly, overlapping OCT scans that were 4.5 mm in length were used to cover the horizontal and vertical meridians up to 9 mm eccentricity from the fovea. At least three OCT scans were obtained at each retinal location. Dense, overlapping SD-OCT raster scans (101 raster lines of 512 A-scans each covering 6 × 6 mm) were performed to sample an 18 × 12-mm region of the retina centered on the fovea. Postacquisition processing of OCT data was performed with custom programs (MatLab ver. 6.5; MathWorks, Natick, MA).

Animals

Shaker1 mice carrying the 4626SB allele, an effective null mutation of *Myo7a*,[41,42] were backcrossed onto the C57BL/6 genetic background and genotyped as described.[9,43] Albino C57Bl/6J-Tyr$^{c\text{-}2J}$ (Jackson Laboratories, Bar Harbor, ME) mice were used as a strain-matched nonpigmented control. All animals were 2 to 3 months old and were maintained on a 12-hour light/12-hour dark cycle, with exposure to 30 to 80 lux of fluorescent lighting during the subjective daytime. Shaker1 homozygous mutants were also distinguished from heterozygous controls by their hyperactivity, head-tossing, and circling behavior. All procedures conformed to institutional animal care and use authorizations and were in accordance with regulations established by the National Institutes of Health and the ARVO Statement for the Use of Animals in Ophthalmic and Vision Research.

Preparation of Whole-Mount Eyecups

Enucleated globes from adult pigmented and albino mice were dissected on ice in Ringer's buffer (130 mM NaCl, 3.6 mM KCl, 2.4 mM $MgCl_2$, 1.2 mM $CaCl_2$, 10 mM HEPES with KOH [pH 7.4], and 20 mM EDTA). Eyecups (the posterior hemisphere) were flattened by making incisions around the rim, and placed on poly-L-lysine-coated microscope slides with the neural retina uppermost. A thin rim of silicon sealant was placed around each eyecup, which was then mounted in PBS and 1% glycerol, with an optical coverslip. Eyecups were then used immediately for microscopy.

Histology and Immunofluorescence Labeling

Eyes for cryosectioning were immersion fixed in cold (−20°C) 90% methanol/10% MES (100 mM MES, 1 mM EGTA, 1 mM $MgSO_4$ [pH 6.9]), rehydrated in PBS and then processed, cryosectioned, and mounted as described previously.[10] Incubation of the retinal sections in 0.1% sodium borohydride in PBS was omitted to prevent quenching of autofluorescence.

Eyecups for immunolabeling were dissected as described earlier, then fixed by immersion in cold 90% methanol/10% MES buffer, rehydrated in 1% goat serum in PBS, and detergent treated with 1% saponin (Sigma-Aldrich, St. Louis, MO) in PBS. They were incubated

overnight at 4°C with the affinity-purified MYO7A antibody pAb2.2[8] diluted in blocking buffer (0.1% saponin, 1% goat serum in PBS), followed by 1 hour at room temperature with Alexa Fluor 594 goat anti-rabbit secondary antibody (Invitrogen, Carlsbad, CA), diluted 1:1000 in blocking buffer. Fluorescent probes against filamentous actin (FITC-phalloidin 1:200; Invitrogen) and DNA (DAPI, 1:10,000 Molecular Probes) were included with the secondary antibody incubation. Labeled eyecups were flat mounted (Mowiol; Calbiochem, San Diego, CA), as described earlier.

Purification of Melanosomes from Mouse RPE Cells

Sheets of RPE cells were isolated from heterozygous shaker1 mouse eyes as described previously,[43] pooled, and stored at −80°C until needed. Highly enriched melanosome fractions purified from RPE sheets were obtained by sequential centrifugation and purification over a 50% iodixanol cushion (Optiprep; Sigma-Aldrich), as described previously.[10,26] The highly-enriched melanosome pellet was resuspended in PBS, mounted on a microscope slide, and either used immediately for microscopy or sealed with varnish and shipped to the other laboratory.

Autofluorescence and Spectral Deconvolution Confocal Microscopy

Multispectral autofluorescent and immunofluorescent datasets were collected from whole-mount eyecups, retinal cryosections, and enriched melanosome fractions by using the 63× oil, plan apochromat, 1.4-NA objective on a spectral deconvolution scanning laser confocal microscope (model FV1000; Olympus, Lake Success, NY), equipped with violet diode (405 nm), argon-ion (457/488/514 nm), krypton-ion (563 nm), and helium-neon ion (633 nm) lasers. Four independent photomultipliers (PMTs) were used for detection of emission spectra. Laser intensity, pinhole diameter, PMT gain, PMT black level, scan speed, and image size were constant for each excitation wavelength between experiments. Laser irradiance levels at the plane of the sample were: 2.5 (405 nm), 1.4 (488 nm), 6 (633 nm), and 1.5 (563 nm) mW. Acquisition was controlled via the integrated software (FluoView; Olympus) software.

AF datasets were acquired at 633-nm excitation, and emission spectra were collected at 10-nm intervals between 700 and 800 nm, using the λ scan function in blind mode. This spectral deconvolution function utilizes calibrated diffraction gratings to provide a variable band-pass emission filter with 2-nm spectral resolution. AF datasets were acquired at 488-nm excitation and emission spectra collected between 500 and 600 nm, 600 and 700 nm, 700 and 800 nm, or 730 and 760 nm. In both cases, emission spectra were collected at wavelengths sufficiently distant from the excitation light to prevent contamination of the emission signals by reflected excitation light. Emission spectra from fluorescent probes were acquired sequentially using the 405/488/563-nm laser lines with the following emission band-pass filters: DAPI (peak 447/BP 60), FITC-phalloidin (536/40), and Alexa Fluor 594 (624/40). Image datasets with associated metadata were exported as 12-bit.oib files. Image analysis, 3-D reconstruction, and montaging were performed with two image-analysis programs (ImageJ; developed by Wayne Rasband, National Institutes of Health, Bethesda, MD; available at http://rsb.info.nih.gov/ij/index.html, and Photoshop CS3; Adobe Systems, Inc., San Jose, CA).

RESULTS

In Vivo Topography of Retinal Disease and NIR-AF in Patients with USH1B

Results from three representative patients with USH1B demonstrated NIR-AF signal topography at different disease stages compared with that in a normal subject (Figs. 1A–D). P1 at age 21 had the mildest disease, with a large expanse of central retina showing an NIR-AF signal distribution that was qualitatively similar to that of the 24-year-old normal subject (Figs. 1A, 1B). There was a bright region of higher NIR-AF signal intensity corresponding to

a 2- to 3-mm diameter region centered on the fovea surrounded by a lower intensity signal extending across the macula.[20,31,36,38] Cross-sectional imaging showed normal lamination of the retina (Figs. 1A, 1B, insets). In P1, retinal degeneration and consequent loss of visual function was apparent nasal to the optic nerve head and at eccentricities greater than ~4 to 5 mm from the fovea (Fig. 1B, arrowheads). P2 at age 11 shows a central region of higher NIR-AF signal surrounded by a lower signal region (Fig. 1C). The ellipsoid boundary apparent on NIR-AF corresponded to the transition zone between detectable and undetectable outer photoreceptor nuclear layer (ONL) thickness apparent on cross-sectional imaging (Fig. 1C, inset). P3 at age 61 demonstrated a more severe stage of USH1B retinal disease. Low NIR-AF signal, forming the background of the image, was interrupted by dark vessels displaying a choroidal pattern (Fig. 1D). Cross-sectional imaging showed a delaminated retina with little evidence of photoreceptors and a substantial increase in choroidal penetration of the NIR scanning light (Fig. 1D, inset).

NIR-AF signal was quantitatively compared to normal results along a linear profile crossing through the foveola and the center of the optic nerve head (Fig. 1E). The profiles of P1 and the normal subject had similar shapes and there was no statistically significant reduction in signal intensity. ONL thickness was within normal limits in P1 and the normal subject across the central region examined (Fig. 1F). In P2, the NIR-AF signal was normal in the central ~4-mm diameter region. Surrounding this region, P2 signal intensities were at or below the lower limit of normal. The ONL thickness in P2 was normal only for the central ~2-mm-diameter region surrounded by an abnormally reduced region. Throughout the central retinal region of P3, NIR-AF signal was abnormally reduced; ONL thickness was reduced to the detection limit of the instrument. These results suggest that significant reductions in NIR-AF intensity colocalize with severe degeneration of photoreceptors in USH1B. The contrast between healthier and more degenerate retinal regions may depend on the signal intensity originating from the choroid, which is thought to correlate with iris color.[31]

Ex Vivo NIR-AF Imaging of Mouse Retinal Sections

Pigmented (C57BL/6) and albino (C57BL/6$^{tyr/tyr}$) mouse eyecups were imaged from semithin cryosections with a spectral deconvolution scanning laser confocal microscope (SDCM) and the 633-nm laser line for red excitation of endogenous fluorophores. AF(ex.633) images of the resulting emission spectra were collected at 10-nm intervals from 700 to 800 nm. In pigmented retinal sections, AF(ex.633) was detected between 730 and 760 nm and localized to the RPE and choroid, as identified by simultaneous DIC imaging (Fig. 2A–C). The AF emission between 730 and 760 nm was reduced greatly in regions of the RPE and choroid containing densely packed melanosomes, suggesting that much of the emission signal was quenched. Since melanosomes absorb ~790-nm light (see Figs. 1, 4), AF emitted from 633-nm excitation could therefore be absorbed by neighboring melanosomes, so that it is likely that the total melanosome-specific AF is significantly underestimated by these imaging conditions. No significant AF(ex.633) originating from the RPE, choroid, or neural retina was detected at the other emission wavelengths (Supplementary Fig. S1; all Supplementary Figures are online at http://www.iovs.org/cgi/content/full/50/9/4386/DC1). SDCM imaging of albino retinal sections under identical conditions did not demonstrate any detectable AF in either the RPE/choroid or the neural retina at 730 to 760 nm (Figs. 2D–F) or any of the other emission wavelengths measured (Supplementary Fig. S1). High-magnification SDCM of pigmented RPE (Figs. 2G–I) was used to demonstrate that the AF(ex.633) signal localized to individual melanosomes, identified by concurrent wide-field differential interference contrast (DIC) imaging.

To define the emission spectrum of the AF(ex.633) signal better, we plotted the average fluorescence intensity from the RPE layer as a function of emission wavelength from

pigmented and albino RPE SDCM datasets (Fig. 2J). Differences in nonspecific autofluorescence between retinal sections, resulting from variations in sample processing were controlled for by subtraction of the average background autofluorescence, directly measured from a region of each retina (the inner plexiform layer) without any melanosomes or known autofluorescent granules present. In pigmented RPE, a major emission peak was identified at 730 to 740 nm with a minor peak at 750 to 760 nm; both peaks were absent from albino RPE. Note that nearly all the melanosomes in the RPE of adult pigmented mice are mature (stage IV), and thus contain melanin; whereas, in albino RPE, lack of tyrosinase activity arrests melanosome biosynthesis before the deposition of the melanin pigment, so that only premelanosomes are present.[23] These results demonstrate that the novel fluorophores identified by AF(Ex.633) imaging require melanin biosynthesis and specifically colocalize with melanosomes, but not with premelanosomes, or other organelles in pigmented RPE.

Melanosome versus Lipofuscin Autofluorescence

For a comparison of the autofluorescence properties of melanosomes with that of lipofuscin, SDCM images were obtained sequentially from the same sections using 488- and 633-nm excitation (Fig. 3). AF emissions with 488-nm excitation, AF(ex.488), were measured over a wide spectrum from 500 to 800 nm and contrasted to emissions with 633-nm excitation, AF (ex.633), over 730 to 760 nm. The maximum AF(ex.488) signal was detected between 500 and 600 nm, predominantly in the RPE and the photoreceptor outer segments (OS; Fig. 3A, Supplementary Fig. S2). This result is in agreement with previous reports describing AF(ex. 488) of lipofuscin peaking between 500 and 600 nm.15›44›45 AF(ex.488) intensity at 600 to 700 nm was detectable but significantly lower (Fig. 3B), consistent with a previous report.[46] Of importance, AF(ex.488) at 700 to 800 nm was reduced to 5% of the emission maximum in the RPE (Fig. 3C) and 2% in the neural retina (Supplementary Fig. S2). No significant AF(ex. 488) signal was detected over the 730 to 760-nm emission range (Fig. 3D), in striking contrast to the strong AF(ex.633) signal emanating from the RPE and choroid (Fig. 3E). Although the AF(ex.488) signal at 500 to 600 nm showed some overlap with the AF(ex.633) signal at 730 to 760 nm, in the RPE, the two are clearly distinct (Fig. 3F). The peak AF(ex.633) is localized to populations of melanosomes in the RPE (most evident apically) and choroid. In contrast, peak AF(ex.488) was found predominantly in the RPE cell body and photoreceptor OS. AF (ex.488) did not localize with melanosomes in the RPE and was absent from the heavily melanized choroidal layer at all emission wavelengths measured, indicating that AF(ex.633) signals represent novel fluorophores specific to melanosomes in the RPE and choroid and are not a result of cross-talk from lipofuscin AF.

NIR-AF Imaging of Purified Melanosomes

To address the specificity of red- and NIR-AF signals, highly enriched fractions of melanosomes, isolated from purified sheets of C57BL/6 RPE, were imaged. The purification method results in an almost pure population of predominantly mature melanosomes with only minor contamination from nuclei, mitochondria, and endosomes/lysosomes.[26] Isolated melanosomes demonstrated strong AF(ex.633) between 730 and 770 nm that was specific for melanosomes identified morphologically by concurrent DIC imaging (Figs. 4A–C). The AF was significantly less at wavelengths below and above this emission band (Supplementary Fig. S3).

For a comparison of the NIR-AF signals collected in vivo with 790-nm excitation, using CSLO, and ex vivo with 633-nm excitation, using SDCM, the same regions of a microscope slide were imaged with both systems at equivalent magnification. Identical clusters of melanosomes showed AF signal with both imaging systems, despite the differences in the wavelength of the excitation light and spectral bands of the collected emission (Figs. 4D–F, 4G–I). These red- and NIR-AF signals were also exceedingly stable, surviving extended illumination on both

systems, as well as transport between our laboratories. Taken together with the data obtained from retinal sections (Figs. 2–3), these results demonstrate that melanosomes are both necessary and sufficient for NIR-AF in RPE cells, and indicate that they are the predominant fluorophores across a relatively broad excitation and emission range, with no significant contribution from other cellular components, including lipofuscin granules or A2E. Thus NIR autofluorescence microscopy provides sensitive and label-free chemical contrast, specific to melanin granules in mature melanosomes.

Detection of Melanosome Position Defects in *Myo7a*-Shaker1 Eyecups

Next, we tested whether AF(ex.633) imaging in shaker1 mouse eyecups would provide sufficient resolution to detect the previously described altered distribution of RPE melanosomes. In shaker1 RPE, the melanosomes are absent from the apical processes, being restricted to the cell body.[9,10] Three-dimensional multispectral SDCM imaging was performed on whole-mount eyecups, isolated from pigmented shaker1 and control littermates. In both control and mutant RPE cells, F-actin was distributed normally. Optical sections through the apical region showed FITC-phalloidin labeling of the apical processes. The melanosome-specific AF(ex.633) was present as discrete puncta in the RPE cell layer of control and mutant whole-mount preparations, and was absent from the adjacent neural retina. However, in optical sections of the RPE apical processes, it was much more evident in control than in mutant RPE (Figs. 5A, 5B). Three-dimensional reconstruction of the apical RPE showed more clearly that, in the mutants compared with controls, the AF(ex.633) signal was absent from the apical processes, which are indicated by the F-actin fluorescence. Instead it was present along the bases of the processes (Fig. 5C, 5D). Quantitative image analysis measuring the peak fluorescence intensity for each channel at each optical section through the RPE layer also identified a significant basal shift in the AF(ex.633) signal in mutants relative to controls, whereas the fluorescence intensity profiles for F-actin were comparable between mutant and control samples (Figs. 5E, 5F). These results agree with the hypothesis that AF(ex.633) between 730 and 760 nm is highly specific for melanosomes in the RPE and can be used effectively to detect defects in the localization of melanosomes without prior labeling.

Imaging NIR-AF in Conjunction with Fluorescently Labeled Proteins

The successful use of AF(ex.633) to identify melanosomes relative to F-actin in whole-mount eyecups with SDCM suggests that this approach could be used with a variety of different fluorescent probes. We therefore imaged whole-mount eyecups that had been colabeled with probes for F-actin (FITC-phalloidin), nuclei (DAPI), and anti-MYO7A (pAb2.2/Alexa594). Images of RPE cells showed that no significant fluorescence cross-talk was evident among the different fluorophores (Supplementary Figs. S4A–D). Hence, AF(ex.633) would be useful for confocal multispectral imaging of multiple cellular probes in conjunction with melanosomes, where the choice of antibodies and exogenous fluorophores may be limited, and where transmitted-light imaging of melanosomes cannot be used (such as in whole-mount preparations).

DISCUSSION

There is a long history of investigation of the role of RPE in the visual process and its relationship with neighboring photoreceptors. [47] Basic science has continually refined our understanding of the RPE, but noninvasive assays of RPE integrity or health in a clinical setting have been mainly limited to low-magnification anatomic description using ophthalmoscopy and angiography, and functional testing by stimulation of the entire eye.[47] With identification of the molecular basis of human ocular diseases has come the prospect of increased understanding of pathogenic mechanisms and treatment of previously incurable human hereditary retinal degenerations.[1–4] It is also now possible to make cellular-level measurements

of the neural retina with state-of-the-art imaging methods,[48–51] but there are very few methods available for in vivo evaluation of individual or groups of RPE cells despite the fact that RPE health is absolutely necessary for the survival of neighboring retinal photoreceptors.[13]

RPE health can be studied with conventional AF imaging using short-wavelength excitation light that takes advantage of the endogenous lipofuscin fluorophores.[15,18] In vivo images of individual RPE cells have been obtained by combining adaptive optics with AF imaging, but the safety of short-wavelength excitation is a concern,[21,52] especially in diseased retinas.[53,54] Longer wavelength light has a better safety profile,[21] and back-scatter intensity[29,30] or polarization properties[55] of NIR light have been used to obtain nonspecific information on RPE health.

A combination of NIR excitation and AF imaging was recently developed.[20,31,32] Endogenous fluorophores contributing to the NIR-AF signal have been postulated to include melanin and melanolipofuscin granules,[20,31,32,36] but fluorescence emissions beyond 700 nm have never been evaluated directly in the neural retina, RPE, or choroid. RPE melanosomes are known to demonstrate only very faint autofluorescence emissions in visible wavelengths (400–700 nm) when excited by short-wavelength (300–500 nm) light.[56] Cutaneous melanin, however, does show an NIR-AF signal.57 A major finding in the present study was the specific attribution of NIR-AF signal to ocular melanosomes in the RPE and choroid. We demonstrated the important finding that lipofuscin granules of the RPE and many other potential fluorophores of the neural retina or the RPE did not contribute detectably to the NIR-AF signal. Thus, NIR-AF imaging can now be added to the limited armamentarium of in vivo methods for the direct and melanosome-specific evaluation of RPE health.

Several molecularly characterized human retinopathies investigated thus far have demonstrated RPE abnormalities corresponding to abnormally high or low NIR-AF signals.[20,33–35] The present work in human USH1B represents the first investigation of a potential bicellular molecular defect in the photoreceptors and the RPE.[9,10,42,43] The ex vivo detectability of defective melanosome localization in the apical RPE of *Myo7a*-null mice attests to the potential sensitivity of the NIR-AF imaging to earliest stages of RPE disease. Assuming that the mutant phenotypes in mouse retina are faithfully represented in human USH1B, our finding of apparently normal NIR-AF in patients at early stages of USH1B disease signals the need for future investigation with advancement of techniques. One possibility may be to include a combination of adaptive optics technology with NIR-AF for cellular-level imaging with subcellular organelle specificity. In the meantime, longitudinal evaluation of different parameters of RPE disease progression with the currently available NIR-AF imaging is likely to be useful for therapeutic interventions intended to modify the natural history of retinal degenerative diseases.

Supplementary Material

Refer to Web version on PubMed Central for supplementary material.

Acknowledgments

The authors thank Xiaodan Song, Malgorzata Swider, Sharon B. Schwartz, Alexander Sumaroka, and Tomas S. Aleman for critical help and the UCSD Human Embryonic Stem Cell Core for the use of the FV1000 confocal microscope.

Supported by grants from the National Eye Institute (EY07042 and EY13203), National Neurovision Research Institute, Foundation Fighting Blindness, Macula Vision Research Foundation, Hope for Vision, Research to Prevent Blindness (RPB), and the Ruth and Milton Steinbach Fund. DSW is a Jules and Doris Stein RPB Professor.

References

1. Bainbridge JW, Smith AJ, Barker SS, et al. Effect of gene therapy on visual function in Leber's congenital amaurosis. N Engl J Med 2008;358:2231–2239. [PubMed: 18441371]
2. Maguire AM, Simonelli F, Pierce EA, et al. Safety and efficacy of gene transfer for Leber's congenital amaurosis. N Engl J Med 2008;358:2240–2248. [PubMed: 18441370]
3. Hauswirth W, Aleman TS, Kaushal S, et al. Treatment of Leber congenital amaurosis due to RPE65 mutations by ocular subretinal injection of adeno-associated virus gene vector: short-term results of a phase I trial. Hum Gene Ther 2008;19:979–990. [PubMed: 18774912]
4. Cideciyan AV, Aleman TS, Boye SL, et al. Human gene therapy for RPE65 isomerase deficiency activates the retinoid cycle of vision but with slow rod kinetics. Proc Natl Acad Sci U S A 2008;105:15112–15117. [PubMed: 18809924]
5. Weil D, Blanchard S, Kaplan J, et al. Defective myosin VIIA gene responsible for Usher syndrome type 1B. Nature 1995;374:60–61. [PubMed: 7870171]
6. Jacobson SG, Aleman TS, Sumaroka A, et al. Disease boundaries in the retina of patients with Usher syndrome caused by MYO7A gene mutations. Invest Ophthalmol Vis Sci 2009;50:1886–1894. [PubMed: 19074810]
7. Hasson T, Heintzelman MB, Santos-Sacchi J, Corey DP, Mooseker MS. Expression in cochlea and retina of myosin VIIa, the gene product defective in Usher syndrome type 1B. Proc Natl Acad Sci USA 1995;92:9815–9819. [PubMed: 7568224]
8. Liu X, Vansant G, Udovichenko IP, Wolfrum U, Williams DS. Myosin VIIa, the product of the Usher 1B syndrome gene, is concentrated in the connecting cilia of photoreceptor cells. Cell Motil Cytoskel 1997;37:240–252.
9. Liu X, Ondek B, Williams DS. Mutant myosin VIIa causes defective melanosome distribution in the RPE of shaker-1 mice. Nat Genet 1998;19:117–118. [PubMed: 9620764]
10. Gibbs D, Azarian SM, Lillo C, et al. Role of myosin VIIa and Rab27a in the motility and localization of RPE melanosomes. J Cell Sci 2004;117:6473–6483. [PubMed: 15572405]
11. Hashimoto T, Gibbs D, Lillo C, et al. Lentiviral gene replacement therapy of retinas in a mouse model for Usher syndrome type 1B. Gene Ther 2007;14:584–594. [PubMed: 17268537]
12. Allocca M, Doria M, Petrillo M, et al. Serotype-dependent packaging of large genes in adeno-associated viral vectors results in effective gene delivery in mice. J Clin Invest 2008;118:1955–1964. [PubMed: 18414684]
13. Bok D. The retinal pigment epithelium: a versatile partner in vision. J Cell Sci Suppl 1993;17:189–195. [PubMed: 8144697]
14. Feeney-Burns L. The pigments of the retinal pigment epithelium. Curr Top Eye Res 1980;2:119–178. [PubMed: 6807609]
15. Delori FC, Dorey CK, Staurenghi G, Arend O, Goger DG, Weiter JJ. In vivo fluorescence of the ocular fundus exhibits retinal pigment epithelium lipofuscin characteristics. Invest Ophthalmol Vis Sci 1995;36:718–729. [PubMed: 7890502]
16. Eldred GE, Katz ML. Fluorophores of the human retinal pigment epithelium: separation and spectral characterization. Exp Eye Res 1988;47:71–86. [PubMed: 3409988]
17. Delori FC, Staurenghi G, Arend O, Dorey CK, Goger DG, Weiter JJ. In vivo measurement of lipofuscin in Stargardt's disease: fundus flavimaculatus. Invest Ophthalmol Vis Sci 1995;36:2327–2331. [PubMed: 7558729]
18. von Ruckmann A, Fitzke FW, Bird AC. Distribution of fundus autofluorescence with a scanning laser ophthalmoscope. Br J Ophthalmol 1995;79:407–412. [PubMed: 7612549]
19. Cideciyan AV, Aleman TS, Swider M, et al. Mutations in ABCA4 result in accumulation of lipofuscin before slowing of the retinoid cycle: a reappraisal of the human disease sequence. Hum Mol Genet 2004;13:525–534. [PubMed: 14709597]
20. Cideciyan AV, Swider M, Aleman TS, et al. Reduced-illuminance autofluorescence imaging in ABCA4-associated retinal degenerations. J Opt Soc Am A Opt Image Sci Vis 2007;24:1457–1467. [PubMed: 17429493]

21. Morgan JI, Hunter JJ, Masella B, et al. Light-induced retinal changes observed with high-resolution autofluorescence imaging of the retinal pigment epithelium. Invest Ophthalmol Vis Sci 2008;49:3715–3729. [PubMed: 18408191]
22. Schraermeyer U, Peters S, Thumann G, Kociok N, Heimann K. Melanin granules of retinal pigment epithelium are connected with the lysosomal degradation pathway. Exp Eye Res 1999;68:237–245. [PubMed: 10068489]
23. Marks MS, Seabra MC. The melanosome: membrane dynamics in black and white. Nat Rev Mol Cell Biol 2001;2:738–748. [PubMed: 11584301]
24. Kennedy CJ, Rakoczy PE, Constable IJ. Lipofuscin of the retinal pigment epithelium: a review. Eye 1995;9:763–771. [PubMed: 8849547]
25. Rozanowski B, Cuenco J, Davies S, et al. The phototoxicity of aged human retinal melanosomes. Photochem Photobiol 2008;84:650–657. [PubMed: 18086241]
26. Azarian SM, McLeod I, Lillo C, Gibbs D, Yates JR, Williams DS. Proteomic analysis of mature melanosomes from the retinal pigmented epithelium. J Proteome Res 2006;5:521–529. [PubMed: 16512666]
27. Elsner AE, Burns SA, Weiter JJ, Delori FC. Infrared imaging of sub-retinal structures in the human ocular fundus. Vision Res 1996;36:191–205. [PubMed: 8746253]
28. Berendschot TT, DeLint PJ, van Norren D. Fundus reflectance: historical and present ideas. Prog Retin Eye Res 2003;22:171–200. [PubMed: 12604057]
29. Jacobson SG, Cideciyan AV, Sumaroka A, et al. Remodeling of the human retina in choroideremia: rab escort protein 1 (REP-1) mutations. Invest Ophthalmol Vis Sci 2006;47:4113–4120. [PubMed: 16936131]
30. Jacobson SG, Cideciyan AV, Aleman TS, et al. Usher syndromes due to MYO7A, PCDH15, USH2A or GPR98 mutations share retinal disease mechanism. Hum Mol Genet 2008;17:2405–2415. [PubMed: 18463160]
31. Keilhauer CN, Delori FC. Near-infrared autofluorescence imaging of the fundus: visualization of ocular melanin. Invest Ophthalmol Vis Sci 2006;47:3556–3564. [PubMed: 16877429]
32. Weinberger AW, Lappas A, Kirschkamp T, et al. Fundus near infrared fluorescence correlates with fundus near infrared reflectance. Invest Ophthalmol Vis Sci 2006;47:3098–3108. [PubMed: 16799056]
33. Cideciyan AV, Aleman TS, Jacobson SG, et al. Centrosomal-ciliary gene CEP290/NPHP6 mutations result in blindness with unexpected sparing of photoreceptors and visual brain: implications for therapy of Leber congenital amaurosis. Hum Mutat 2007;28:1074–1083. [PubMed: 17554762]
34. Aleman TS, Cideciyan AV, Sumaroka A, et al. Retinal laminar architecture in human retinitis pigmentosa caused by rhodopsin gene mutations. Invest Ophthalmol Vis Sci 2008;49:1580–1590. [PubMed: 18385078]
35. Herrera W, Aleman TS, Cideciyan AV, et al. Retinal disease in Usher syndrome III caused by mutations in the clarin-1 gene. Invest Ophthalmol Vis Sci 2008;49:2651–2660. [PubMed: 18281613]
36. Kellner U, Kellner S, Weber BH, Fiebig B, Weinitz S, Ruether K. Lipofuscin- and melanin-related fundus autofluorescence visualize different retinal pigment epithelial alterations in patients with retinitis pigmentosa. Eye 2009;23:1349–1359. [PubMed: 18791550]
37. Kellner U, Kellner S, Weinitz S. Chloroquine retinopathy: lipofuscin- and melanin-related fundus autofluorescence, optical coherence tomography and multifocal electroretinography. Doc Ophthalmol 2008;116:119–127. [PubMed: 18080820]
38. Theelen T, Boon CJ, Klevering BJ, Hoyng CB. Fundus autofluorescence in patients with inherited retinal diseases: patterns of fluorescence at two different wavelengths (in German). Ophthalmologe 2008;105:1013–1022. [PubMed: 18415102]
39. Huang Y, Cideciyan AV, Papastergiou GI, et al. Relation of optical coherence tomography to microanatomy in normal and rd chickens. Invest Ophthalmol Vis Sci 1998;39:2405–2416. [PubMed: 9804149]
40. Jacobson SG, Cideciyan AV, Aleman TS, et al. Photoreceptor layer topography in children with Leber congenital amaurosis caused by RPE65 mutations. Invest Ophthalmol Vis Sci 2008;49:4573–4577. [PubMed: 18539930]

41. Hasson T, Walsh J, Cable J, Mooseker MS, Brown SD, Steel KP. Effects of shaker-1 mutations on myosin-VIIa protein and mRNA expression. Cell Motil Cytoskeleton 1997;37:127–138. [PubMed: 9186010]
42. Liu X, Udovichenko IP, Brown SDM, Steel KP, Williams DS. Myosin VIIa participates in opsin transport through the photoreceptor cilium. J Neurosci 1999;19:6267–6274. [PubMed: 10414956]
43. Gibbs D, Kitamoto J, Williams DS. Abnormal phagocytosis by retinal pigmented epithelium that lacks myosin VIIa, the Usher syndrome 1B protein. Proc Natl Acad Sci U S A 2003;100:6481–6486. [PubMed: 12743369]
44. Boulton M, Rozanowska M, Rozanowski B, Wess T. The photoreactivity of ocular lipofuscin. Photochem Photobiol Sci 2004;3:759–764. [PubMed: 15295632]
45. Sparrow JR, Parish CA, Hashimoto M, Nakanishi K. A2E, a lipofuscin fluorophore, in human retinal pigmented epithelial cells in culture. Invest Ophthalmol Vis Sci 1999;40:2988–2995. [PubMed: 10549662]
46. Marmorstein AD, Marmorstein LY, Sakaguchi H, Hollyfield JG. Spectral profiling of autofluorescence associated with lipofuscin, Bruch's Membrane, and sub-RPE deposits in normal and AMD eyes. Invest Ophthalmol Vis Sci 2002;43:2435–2441. [PubMed: 12091448]
47. Marmor, MF.; Wolfensberger, TJE. The Retinal Pigment Epithelium. New York: Oxford University Press; 1998.
48. Carroll J, Neitz M, Hofer H, Neitz J, Williams DR. Functional photoreceptor loss revealed with adaptive optics: an alternate cause of color blindness. Proc Natl Acad Sci U S A 2004;101:8461–8466. [PubMed: 15148406]
49. Zawadzki RJ, Cense B, Zhang Y, Choi SS, Miller DT, Werner JS. Ultrahigh-resolution optical coherence tomography with monochromatic and chromatic aberration correction. Opt Express 2008;16:8126–8143. [PubMed: 18545525]
50. Fernandez EJ, Hermann B, Povazay B, et al. Ultrahigh resolution optical coherence tomography and pancorrection for cellular imaging of the living human retina. Opt Express 2008;16:11083–11094. [PubMed: 18648422]
51. Potsaid B, Gorczynska I, Srinivasan VJ, et al. Ultrahigh speed spectral/Fourier domain OCT ophthalmic imaging at 70,000 to 312,500 axial scans per second. Opt Express 2008;16:15149–15169. [PubMed: 18795054]
52. Morgan JI, Dubra A, Wolfe R, Merigan WH, Williams DR. In vivo autofluorescence imaging of the human and macaque retinal pigment epithelial cell mosaic. Invest Ophthalmol Vis Sci 2009;50:1350–1359. [PubMed: 18952914]
53. Cideciyan AV, Jacobson SG, Aleman TS, et al. In vivo dynamics of retinal injury and repair in the rhodopsin mutant dog model of human retinitis pigmentosa. Proc Natl Acad Sci U S A 2005;102:5233–5238. [PubMed: 15784735]
54. Delori FC, Webb RH, Sliney DH. Maximum permissible exposures for ocular safety (ANSI 2000), with emphasis on ophthalmic devices. J Opt Soc Am A Opt Image Sci Vis 2007;24:1250–1265. [PubMed: 17429471]
55. Gotzinger E, Pircher M, Geitzenauer W, et al. Retinal pigment epithelium segmentation by polarization sensitive optical coherence tomography. Opt Express 2008;16:16410–16422. [PubMed: 18852747]
56. Boulton M, Docchio F, Dayhaw-Barker P, Ramponi R, Cubeddu R. Age-related changes in the morphology, absorption and fluorescence of melanosomes and lipofuscin granules of the retinal pigment epithelium. Vision Res 1990;30:1291–1303. [PubMed: 2219746]
57. Huang Z, Zeng H, Hamzavi I, et al. Cutaneous melanin exhibiting fluorescence emission under near-infrared light excitation. J Biomed Opt 2006;11:34010. [PubMed: 16822060]

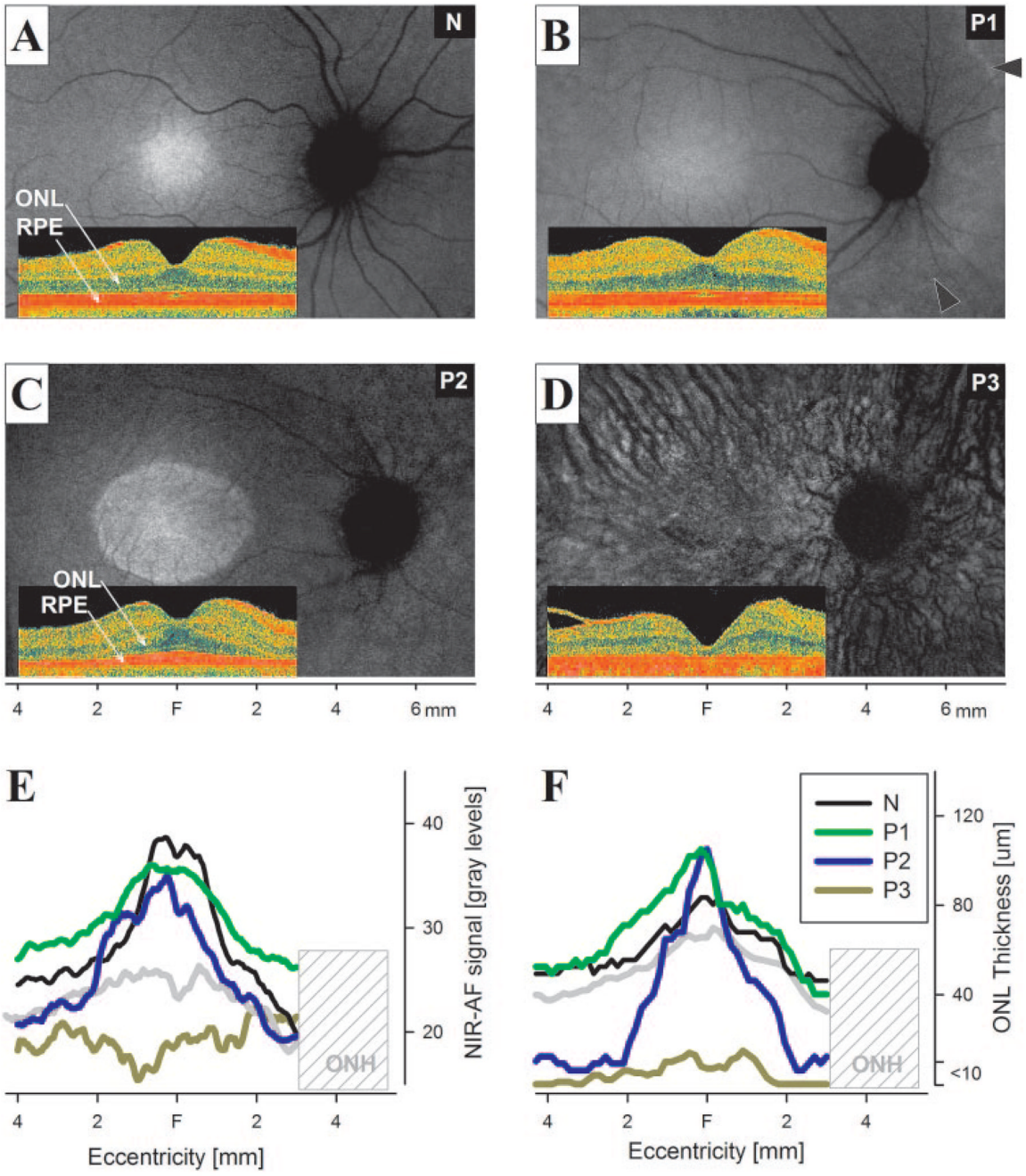

FIGURE 1.

NIR-AF images of normal subjects and USH1B patients. (**A**–**D**) NIR-AF images of a representative normal (N, age 24; green iris), and USH1B-affected patients P1 (age 21; green iris), P2 (age 11; light brown iris), and P3 (age 61; hazel iris) at different stages of disease. Images are individually contrast-stretched for visibility of features. *Arrowheads*: transition zone apparent between the more preserved central retina and the degenerating peripheral retina. *Insets:* cross-sectional SD-OCT images obtained along the horizontal meridian. NIR-AF signal intensity (**E**) and ONL thickness (**F**) measurements along the horizontal profile localized the correspondence between photoreceptor loss and AF abnormalities. The lower limit of normal

(mean −2 SD) is shown in each panel (*gray trace*). *Hashed area*: the nasal retinal region corresponding to the variable location of the optic nerve head (ONH) in different eyes.

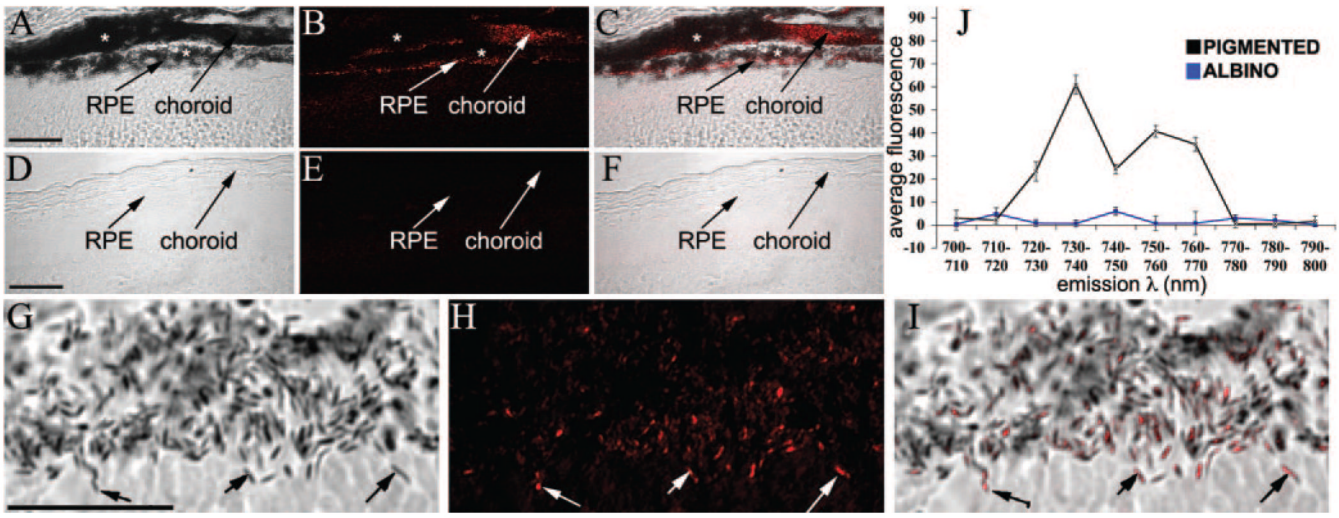

FIGURE 2.

Confocal spectral detection of AF(ex.633) in mouse retina/RPE sections. (**A**–**C**) Pigmented and (**D**–**F**) albino retinas. Emission wavelengths were 730 to 760 nm. DIC images merged with the peak AF(ex.633) are shown for comparison. (**G**–**I**) Higher magnification SDCM micrographs illustrate colocalization of AF(ex.633) with melanosomes. *Arrows*: colocalization of AF with melanosomes. (⋆) Regions of densely packed melanosomes, yet low AF, which was probably due to the quenching of the emission signal by secondary absorbance. (**J**) AF (ex.633) fluorescence intensity was plotted against emission wavelength for pigmented (*black*) and albino (*blue*) RPE. A major fluorescence peak at 730 to 740 nm and a minor peak at 750 to 760 nm were present in pigmented RPE, but were absent in nonpigmented RPE (n = 3). Scale bars, 25 μm.

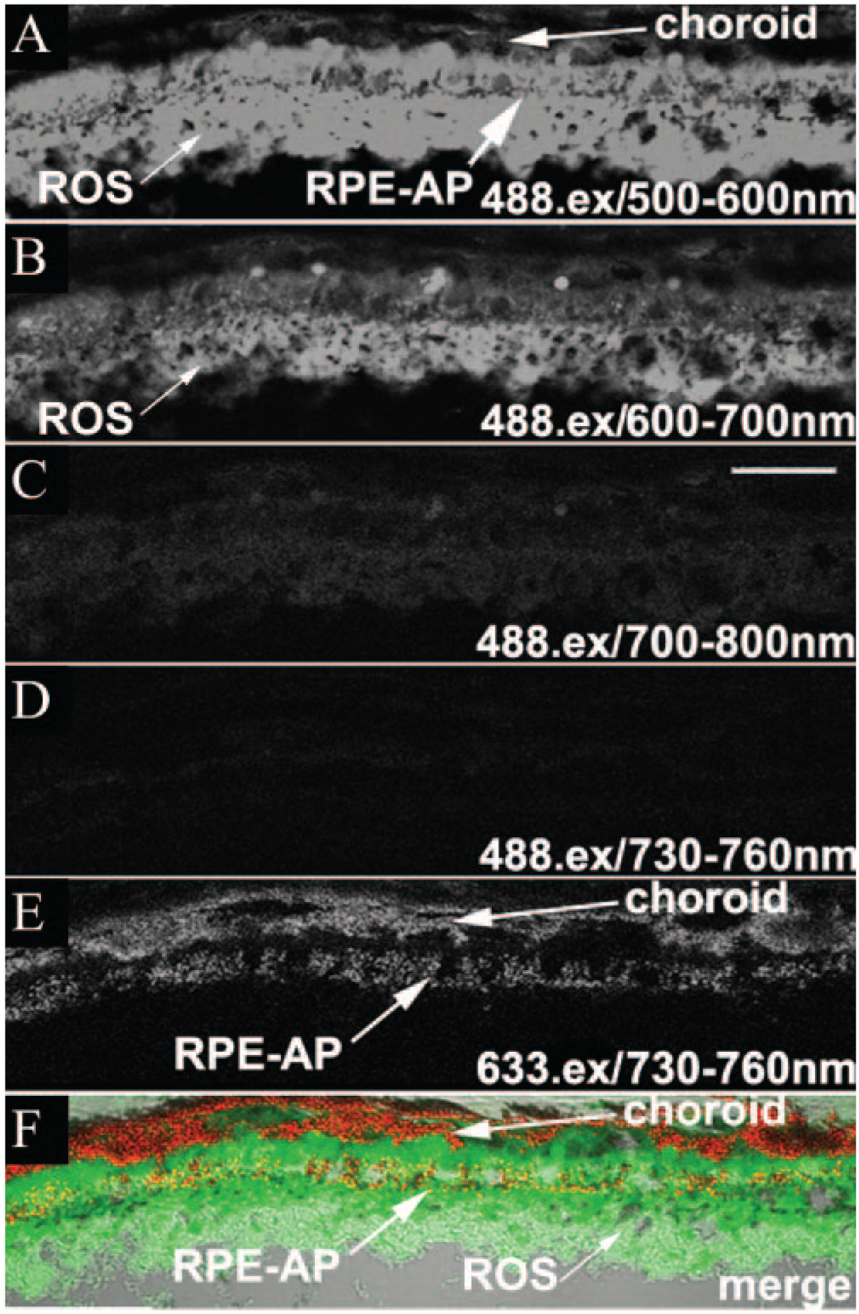

FIGURE 3.

AF(ex.488) images from mouse RPE sections. Emission wavelengths are 500 to 600 (**A**), 600 to 700 (**B**), 700 to 800 (**C**) and 730 to 760 (**D**, **F**) nm. (**E**) A peak AF(ex.633) image is shown for comparison. (**F**) A merged image comparing the localization of peak AF(ex.488) (*green*), peak AF(ex.633) (*red*), and melanosomes (DIC). Although there was overlap, the AF(ex.488) and AF(ex.633) signals were clearly distinct, with the AF(ex.633) associated with the melanosomes. RPE-AP, apical RPE. Scale bar, 25 μm.

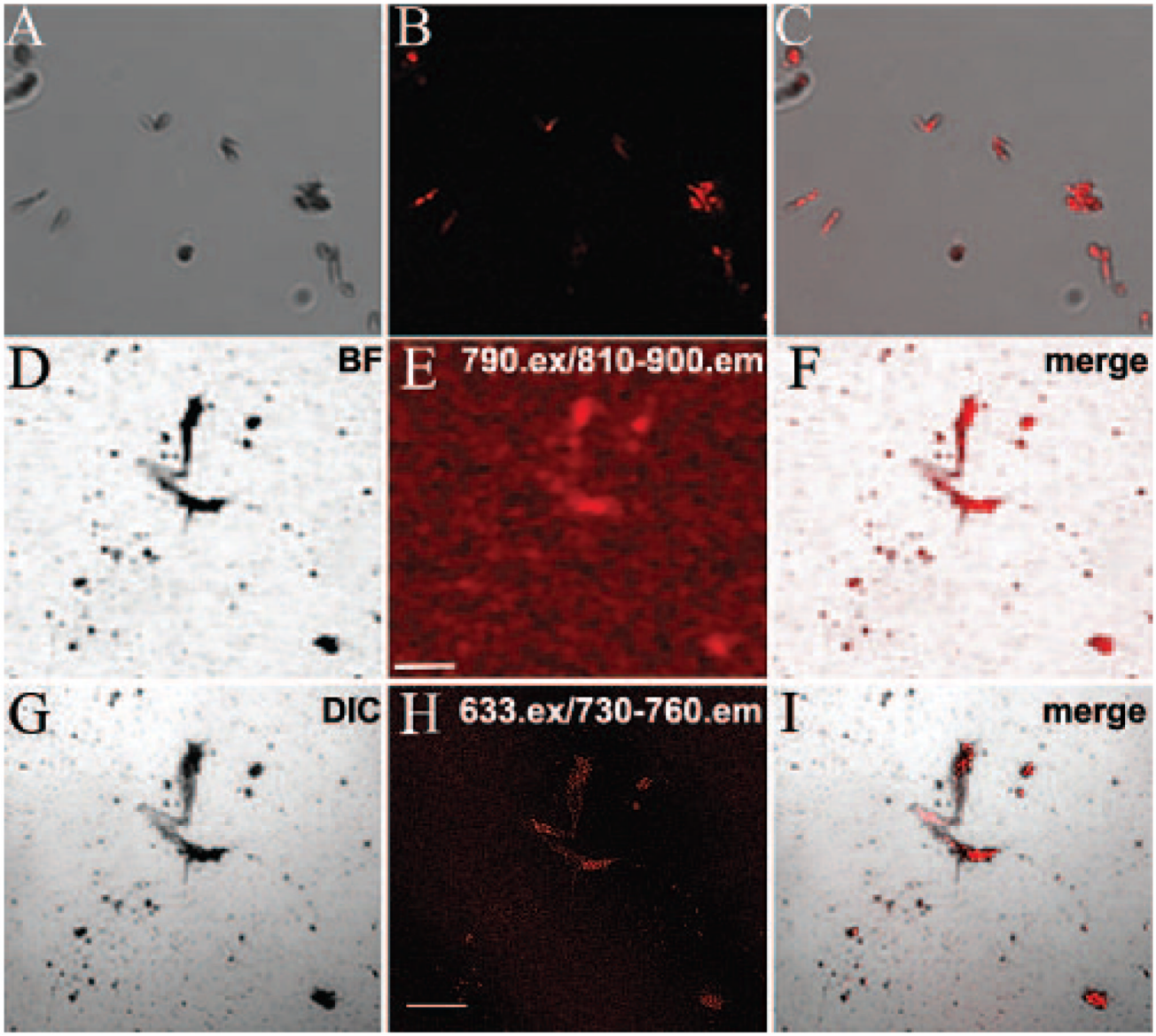

FIGURE 4.

AF imaging of purified melanosomes isolated from mouse RPE sheets. (**A**–**C**) DIC and confocal micrographs of peak AF(ex.633) emission, illustrating colocalization between melanosomes and peak AF(ex.633). (**D**–**I**) Low-magnification AF imaging, using either CSLO (**D**–**F**) or SDCM (**G**–**I**), to image the same region of a microscope slide containing isolated melanosomes. Slides were shipped between laboratories; in this case, the "inverted T" signature of melanosomes clustered with cellular debris (evident in the center) was used to help identify the given region. Comparable AF patterns are apparent with either AF(ex.790) or AF(ex.633) (**E**, **H**). Scale bar, 100 μm.

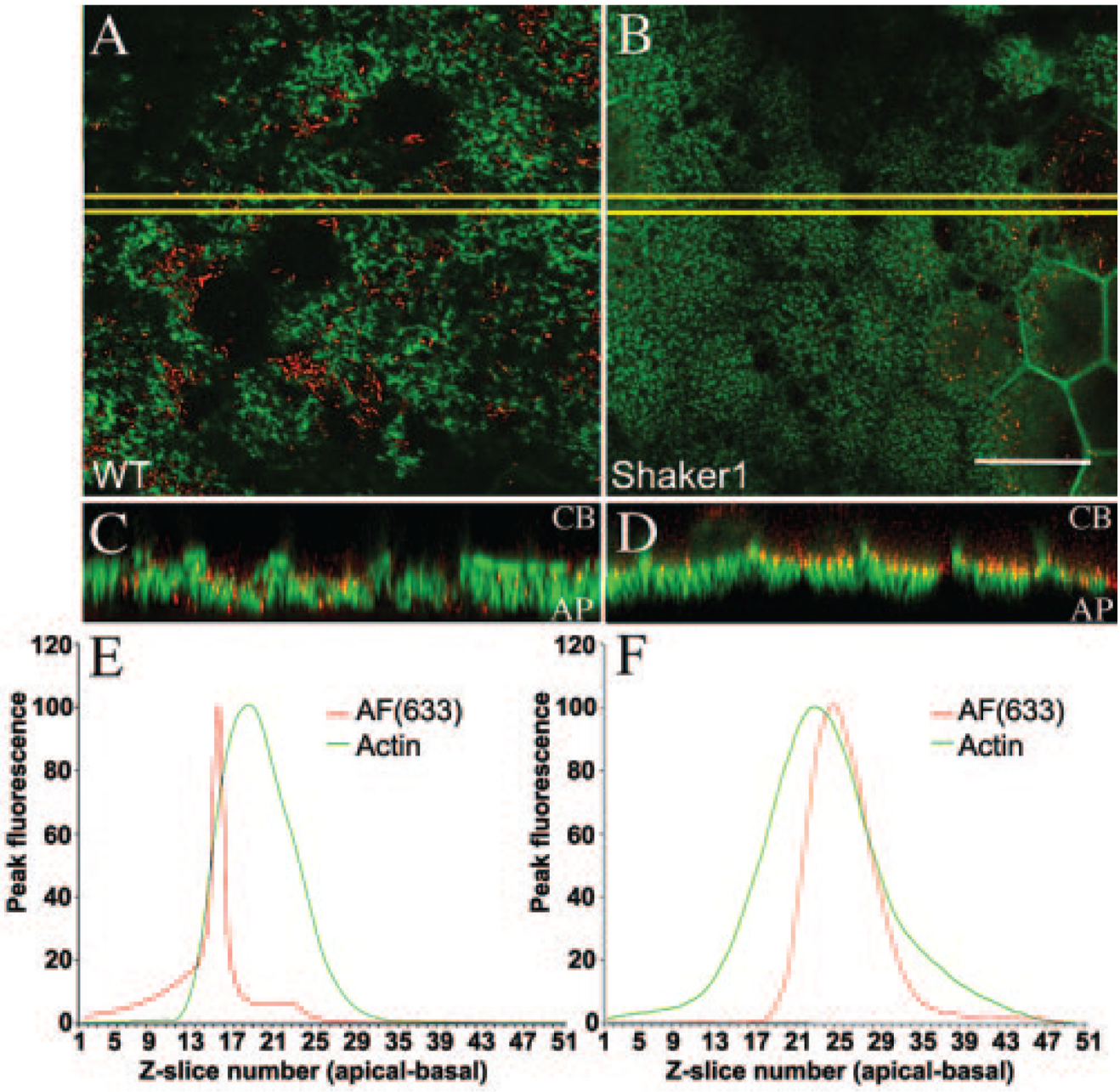

FIGURE 5.

AF(ex.633) imaging of melanosomes in *Myo7a*-null RPE. Confocal microscopy of whole-mount eyecups, showing single optical sections through the apical processes of control (**A**) and mutant (**B**) RPE. AF(ex.633) emitting at 730 to 760 nm is shown in *red* and FITC-phalloidin labeling of F-actin in *green*. The mutant image is slightly oblique. AF was evident only on the *right* part of the image, where it passed into the cell body. Boxed regions (*yellow*) were used for 3-D reconstruction to generate 90°-rotated projections of control (**C**) and mutant (**D**) apical RPE. AF(ex.633) signals in the control were evident throughout the apical F-actin region. By contrast, they are distributed only along the basal aspect of this region in the mutant. Quantification of AF(ex.633) (*red*) and FITC-phalloidin (*green*) fluorescence intensities along the *z*-axis of control (**E**) and mutant (**F**) apical RPE showed no significant change in actin

localization, but a significant basal shift of AF(ex.633) in mutant compared with the control. Scale bar, 25 μm.